


Implementation and investigation of electron-nucleus scattering in NEUT neutrino event generator

Seisho Abe 

*Kamioka Observatory, Institute for Cosmic Ray Research,
University of Tokyo, Kamioka, Gifu 506-1205, Japan**

(Dated: December 11, 2024)

Understanding nuclear effects is essential for improving the sensitivity of neutrino oscillation measurements. Validating nuclear models solely through neutrino scattering data is challenging due to limited statistics and the broad energy spectrum of neutrinos. In contrast, electron scattering experiments provide abundant high-precision data with various monochromatic energies and angles. Since both neutrinos and electrons interact via electroweak interactions, the same nuclear models can be applied to simulate both interactions. Thus, high-precision electron scattering data is essential for validating the nuclear models used in neutrino experiments. To enable this, the author has newly implemented electron scattering in the NEUT neutrino event generator, covering two interaction modes: quasielastic (QE) and single pion production. NEUT predictions of QE agree well with numerical calculations, supporting the validity of this implementation. From comparisons with NEUT predictions and inclusive electron scattering data, the momentum-dependent binding energy correction is derived, corresponding to effects beyond the plane wave impulse approximation. The impact of this correction on neutrino interactions is also evaluated. Significant differences in charged lepton kinematics are observed, with approximately 20 MeV of peak shift in the reconstructed neutrino energy distribution, which is important for accurately measuring neutrino oscillation parameters. It is expected to serve as a foundation for future discussions on electron scattering using NEUT.

I. INTRODUCTION

Neutrino-nucleus interaction is one of the dominant systematic uncertainties in measuring neutrino oscillation parameters [1, 2]. The neutrino energy is reconstructed using measured particle kinematics. This analysis relies on neutrino-nucleus interaction modeling, which involves complex multi-body physics processes. Various neutrino experiments measure and constrain the models, but substantial uncertainties remain [3]. The difficulties mainly arise from two factors. First, we have limited statistics due to the small neutrino cross section. Neutrino detectors are typically large to gather sufficient statistics, but coarse measurements around the target nucleus. Second, neutrino fluxes usually have broad energy spectra because they are produced by pion and kaon decay in flight. There are several exceptions using neutrinos from kaon decay at rest [4, 5]. However, we cannot generate neutrinos with monochromatic energy at arbitrary energies.

Electron scattering can overcome these difficulties due to the availability of many high-precision datasets with different monochromatic electron energies and scattering angles. Since both electrons and neutrinos interact via electroweak interactions, their scattering processes and formalisms are similar: Electrons interact with nucleons through vector currents, while neutrinos interact via both vector and axial vector currents. Therefore, the same framework can be employed to simulate neutrino-nucleon and electron-nucleon scatterings. This approach enables

the validation of nuclear models used in neutrino-nucleus interaction through abundant electron scattering data.

Extensions of neutrino event generators to electron scattering have been actively discussed in recent years. GENIE [6, 7] has incorporated electron scattering since version 2 covering all major interaction channels: quasielastic (QE), resonance pion production (RES), deep inelastic scattering, and meson-exchange current. NuWro offers electron scattering referred to as eWro [8]. This primarily focuses on QE while also supporting single pion production (1π) with different treatments of the nonresonance background compared to NuWro. NuWro recently introduced an updated simulation for QE electron scattering presented in Ref. [9]. A new theory-driven lepton event generator ACHILLES [10] offers neutrino and electron scatterings. The interaction channel is currently limited to QE only. GiBUU [11] provides a unified theory and transport framework capable of simulating electron-nucleus scattering. There are also several discussions of numerical calculation in Refs. [12–14], which are also useful for validating implementations of event generators.

An implementation of electron scattering in NEUT [15] was previously developed by McElwee *et al.* [16, 17]. This implementation was limited to QE based on spectral function (SF) developed by Benhar *et al.* [18, 19] and was not incorporated in the distributed version of NEUT. The author newly implemented electron scattering following the NEUT framework so that it can be integrated into the NEUT standard distribution. As well as QE interactions, 1π based on the DCC model [20, 21] is also implemented. This paper presents the new implementation of electron scattering in NEUT and the initial validations and investigations using experimental data.

This paper is organized as follows: Section II describes

* seisho@icrr.u-tokyo.ac.jp

the formalism of electron-nucleus scattering; Section III presents comparisons with inclusive electron scattering data; and Section IV demonstrates the impact of binding energy correction obtained from electron scattering on neutrino interactions. Note that our code is not included in the latest NEUT version 5.8.0. It is expected to be included in the upcoming version 5.9.0.

II. FORMALISM

The formalism of neutrino and electron scattering in NEUT is based on the plane wave impulse approximation (PWIA), which neglects the distortion of the struck nucleon wave function by nuclear potential.

A. Quasielastic interactions based on the spectral function

Several nuclear models are implemented for QE interactions in NEUT. A model based on the SF developed by Benhar *et al.* [18, 19] is extended to electron scattering. The implementation for neutrino interactions is based on NuWro [22] with several improvements by Furmanski [23]. The author then made several further modifications. Due to the similarities between neutrino and electron interactions, we can describe both interactions within the same formalism by changing the coupling constant and form factors. A comprehensive formalism of neutrino and electron QE interactions is summarized in this section.

Figure 1 shows a diagram and variable notation of QE scattering on bound nucleon. The energy transfer ω , the three-momentum transfer \mathbf{q} , and the squared of four-momentum transfer Q^2 can be written as follows:

$$\begin{aligned}\omega &= E_k - E_{k'}, \\ \mathbf{q} &= \mathbf{k} - \mathbf{k}', \\ Q^2 &= -q^2 = -\omega^2 + \mathbf{q}^2.\end{aligned}\quad (1)$$

Similarly, we can define the following parameters from nucleon kinematics:

$$\begin{aligned}\tilde{\omega} &= E_{p'} - E_p, \\ \tilde{Q}^2 &= -\tilde{q}^2 = -\tilde{\omega}^2 + (\mathbf{p}' - \mathbf{p})^2 = -\tilde{\omega}^2 + \mathbf{q}^2, \\ E_p &= \sqrt{M^2 + \mathbf{p}^2},\end{aligned}\quad (2)$$

since $\mathbf{k} + \mathbf{p} = \mathbf{k}' + \mathbf{p}'$ from momentum conservation. Note that the energy of target nucleon E_p uses an on-shell nucleon mass M . From the energy conservation, we can get

$$E_k + M_{Atom} = E_{k'} + E_{A-1} + E_{p'}, \quad (3)$$

where M_{Atom} is the target nucleus mass and E_{A-1} is the energy of residual nucleus. The removal energy \tilde{E} can be defined as

$$\tilde{E} = E_k - E_{k'} - E_{p'} + M = \omega + M - E_{p'}. \quad (4)$$

We can get the momentum-dependent binding energy ϵ_B :

$$\epsilon_B = \omega - \tilde{\omega} = \tilde{E} + E_p - M. \quad (5)$$

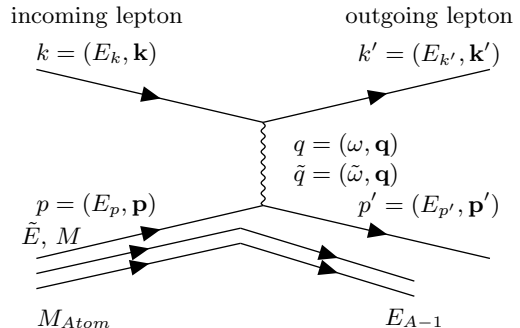


FIG. 1. Diagram and variable notation for quasielastic scattering on bound nucleon. Nucleons other than the target are treated as spectators in the assumption of the plane wave impulse approximation.

The total cross section is given by the following equation under the assumption of the PWIA:

$$\frac{d\sigma_{\text{tot}}}{dQ^2} = \int d^3p d\tilde{E} P_{\text{hole}}(\mathbf{p}, \tilde{E}) \frac{d\sigma}{dQ^2}, \quad (6)$$

where $P_{\text{hole}}(\mathbf{p}, \tilde{E})$ represents the probability of removing a nucleon with momentum \mathbf{p} and removal energy \tilde{E} , given by the SF. And $d\sigma/dQ^2$ denotes the elementary cross section:

$$\frac{d\sigma}{dQ^2} = \frac{C}{E_k} \int d^3k' \delta(\omega + M - \tilde{E} - E_{p'}) \frac{L_{\mu\nu} H^{\mu\nu}}{E_p E_{p'} E_{k'}}, \quad (7)$$

where the $L_{\mu\nu}$ and $H^{\mu\nu}$ represent leptonic and hadronic tensors, respectively. The coupling constant C can be written as follows for charged-current (CC), neutral-current (NC), and electromagnetic (EM) interactions:

$$C = \begin{cases} \frac{G_F^2 \cos^2 \theta_C}{8\pi^2} & (\text{CC}), \\ \frac{G_F^2}{8\pi^2} & (\text{NC}), \\ \frac{\alpha^2}{Q^4} & (\text{EM}), \end{cases} \quad (8)$$

where the Fermi constant $G_F = 1.16639 \times 10^{-11} / \text{MeV}^2$, the fine structure constant $\alpha = 7.299 \times 10^{-3}$, and the Cabibbo angle θ_C with $\cos \theta_C = 0.97418$. Since the massless photon mediates the EM, the factor of $1/Q^4$ appears. The elementary cross section includes the integral of outgoing lepton momentum d^3k' . In NEUT event generation procedure, it is converted to the center-of-mass variables as described in Appendix A.

The leptonic and hadronic tensors $L_{\mu\nu} H^{\mu\nu}$ can be written as

$$L_{\mu\nu} H^{\mu\nu} = 2 \sum_{j=1}^5 A_j W_j, \quad (9)$$

where A_j is given by

$$\begin{aligned}
A_1 &= 2M^2 k \cdot k', \\
A_2 &= 2p \cdot k \ p \cdot k' - p^2 k \cdot k', \\
A_3 &= k \cdot \tilde{q} \ k' \cdot p - k \cdot p \ k' \cdot \tilde{q}, \\
A_4 &= k \cdot k' \ \tilde{q}^2 - 2k \cdot \tilde{q} \ k' \cdot \tilde{q}, \\
A_5 &= k \cdot p \ k' \cdot \tilde{q} + k' \cdot p \ k \cdot \tilde{q} - k \cdot k' \ p \cdot \tilde{q},
\end{aligned} \tag{10}$$

and W_j can be expressed as

$$\begin{aligned}
W_1 &= (F_A)^2(1 + \tau) + \tau(F_1 + F_2)^2, \\
W_2 &= (F_A)^2 + (F_1)^2 + \tau[(F_2)^2 + 4(F_{3A})^2], \\
W_3 &= \pm 2F_A(F_1 + F_2), \\
W_4 &= \frac{1}{4}[(F_2)^2 - \tau(F_2 - 2F_{3V})^2 - 4\tau(F_P + F_{3A})^2] \\
&\quad - (F_{3V})^2 - \frac{1}{2}[F_1(2F_{3V} - F_2) - 2F_A(F_P + F_{3A})], \\
W_5 &= W_2 \pm 2[F_{3V}(F_1 - \tau F_2) - F_{3A}(F_A - 2\tau F_P)],
\end{aligned} \tag{11}$$

with $\tau = -\tilde{q}^2/(4M^2)$ (Ref. [24]). The upper (lower) sign corresponds to neutrino (antineutrino). The second-class form factors are tuned off by default: $F_{3A} = F_{3V} = 0$. The axial vector form factor F_A and the pseudo-scalar form factor F_P for CC, NC, and EM interactions can be expressed as follows, assuming dipole parameterization (Ref. [25]):

$$\begin{aligned}
F_A^{\text{CC}} &= g_A \left(1 + \frac{\tilde{Q}^2}{M_A^2}\right)^{-2}, \\
F_A^{\text{NC}} &= \frac{1}{2}(\pm F_A^{\text{CC}} + F_A^s) \\
&= \frac{1}{2}(\pm g_A + g_A^s) \left(1 + \frac{\tilde{Q}^2}{M_A^2}\right)^{-2}, \\
F_P^{\text{CC,NC}} &= \frac{2M^2}{m_\pi^2 + \tilde{Q}^2} F_A^{\text{CC,NC}}, \\
F_A^{\text{EM}} &= F_P^{\text{EM}} = 0,
\end{aligned} \tag{12}$$

where the axial coupling constant is $g_A = -1.2673$ and the axial mass is $M_A = 1.21$ GeV by default. The upper (lower) sign corresponds to the proton (neutron) form factors. The strange axial coupling constant g_A^s is known to prefer negative values [26–29]. NEUT sets $g_A^s = 0$ by default, neglecting the strange quark contribution. The vector form factors for CC, NC, and EM interactions can

be written as

$$\begin{aligned}
F_{1,2}^{\text{CC}} &= F_{1,2}^p - F_{1,2}^n, \\
F_{1,2}^{\text{NC,p/n}} &= \pm \frac{1}{2} F_{1,2}^{\text{CC}} - 2 \sin^2 \theta_W F_{1,2}^{p/n}, \\
F_1^{p/n} &= \frac{G_E^{p/n} + \tau G_M^{p/n}}{1 + \tau}, \\
F_2^{p/n} &= \frac{G_M^{p/n} - G_E^{p/n}}{1 + \tau}, \\
F_1^{\text{EM,p/n}} &= \frac{G_E^{p/n} + \tau G_M^{p/n}}{1 + \tau}, \\
F_2^{\text{EM,p/n}} &= \frac{G_M^{p/n} - G_E^{p/n}}{1 + \tau},
\end{aligned} \tag{13}$$

where $G_E^{p/n}$ and $G_M^{p/n}$ are Sachs form factors, and θ_W is the Weinberg angle, where $\sin^2 \theta_W = 0.231$. The upper (lower) sign of the NC form factor corresponds to the proton (neutron). The strangeness contributions of the vector form factors are consistent with zero [26], thus it is neglected in Eq. (13). There are several parameterizations for the Sachs form factors. A simple dipole parameterization can be written as

$$\begin{aligned}
\frac{G_M^p}{\mu_p} &= \frac{G_M^n}{\mu_n} = G_E^p = D, \\
D &= \left(1 + \frac{\tilde{Q}^2}{M_V^2}\right)^{-2}, \\
G_E^n &= 0,
\end{aligned} \tag{14}$$

where $\mu_p = 2.793$ and $\mu_n = -1.913$ for the magnetic moments of proton and neutron, and $M_V = 0.84$ GeV for vector mass. For subsequent calculations using NEUT, we employed a more sophisticated parameterization, BBBA05 [30], derived from electron scattering data.

Pauli blocking is implemented using a simple step function, which requires the momentum of the outgoing nucleon to exceed the Fermi surface p_F : $|\mathbf{p}'| > p_F$. NEUT uses $p_F = 209$ MeV for ^{12}C and ^{16}O by default, which is the average Fermi momentum calculated from nuclear density distributions [19]. In the case of CC and EM interactions, the Coulomb potential $|V_{eff}|$ take effects. NEUT currently considers this effect only for EM. The effect of the Coulomb potential is considered by

$$\begin{aligned}
E_k &= E_0 + |V_{eff}|, \\
E'_k &= E'_0 + |V_{eff}|,
\end{aligned} \tag{15}$$

where E_0 (E'_0) is the incoming (outgoing) electron energy at a sufficient distance from the nucleus. NEUT sets a constant value of $|V_{eff}| = 3.1$ MeV and 3.4 MeV for ^{12}C and ^{16}O , respectively [12, 31].

Figure 2 shows QE cross sections of CC, NC, and EM interactions. Note that NEUT employs a cut-off of $Q^2 > 0.01$ GeV² in Eq. (6) for EM interaction to increase simulation speed. The NCQE model explained

here is different from that discussed in the past Super-Kamiokande analysis [32–34]. They used the cross section calculated with different parameters $g_A^s = -0.08$ [35] and different code written by the authors of Refs. [36, 37]. A good consistency is confirmed in the cross section when $g_A^s = -0.08$ is used in this model. The cross sections have statistical fluctuation arising from the limited number of calculation trials. In event generation, these cross section data are interpolated to make it less effective for the simulation.

The tensors written in Eqs. (10) and (11) are based on an approximation, called the de Forest prescription [38]. In this approximation, we use the same expression as the target nucleon has on-shell mass M while assuming the outgoing nucleon gains only a part of the energy transfer as also mentioned in Ref. [24]. This is realized by using \tilde{Q}^2 and \tilde{q} instead of Q^2 and q in the tensor calculations. When the target nucleon is unbound, \tilde{q} and q become equivalent. Then, A_4 can be written as

$$A_4 = \frac{1}{2}(q^2 - m^2)m^2. \quad (16)$$

We obtain $A_4 = 0$ in the case of NC ($m \rightarrow 0$). The pseudo-scalar form factor F_P only appears in W_4 when the second-class form factors are absent. Therefore, in the case of an unbound nucleon target, the pseudo-scalar form factor F_P does not contribute to the NC cross section. The same conclusion can be confirmed by the Llewellyn-Smith formalism [39], which describes interaction with unbound nucleon. In contrast, for a bound nucleon, A_4 has a non-zero value because of the presence of binding energy ϵ_B . Consequently, the pseudo-scalar form factor F_P contributes to the NC cross section, approximately 3%.

The SF $P_{\text{hole}}(\mathbf{p}, \tilde{E})$ consists of two components: a mean-field term and a correlated term. In NEUT framework, the mean-field term corresponds to $|\mathbf{p}| < 300$ MeV and $\tilde{E} < 100$ MeV, while the correlated term corresponds to the remaining phase space. It should be noted that the correlated term also contributes to $|\mathbf{p}| < 300$ MeV and $\tilde{E} < 100$ MeV as shown in Ref. [40]. However, NEUT currently does not distinguish this contribution from the mean-field term. The correlated term gives a tail in momentum and removal energy, contributing approximately 20% to the total. Interactions involving a correlated nucleon are considered to be accompanied by the emission of an additional paired nucleon. The nucleon pair ratios (pp , nn , pn) have been measured in electron scattering experiments [41, 42]. Approximately $90 \pm 10\%$ of correlated pairs are pn while pp and nn have equal contributions of $5 \pm 1.5\%$ under the assumption of isospin symmetry. NEUT assumes 100% of the correlated pairs are pn by default. The struck nucleon, along with any correlated nucleon pairs, subsequently undergoes the final-state interactions (FSI), which is described by the intranuclear cascade model explained in Ref. [15]. NEUT provides two nuclear deexcitation models. One is a simple data-driven model based on Ref. [43] employed by

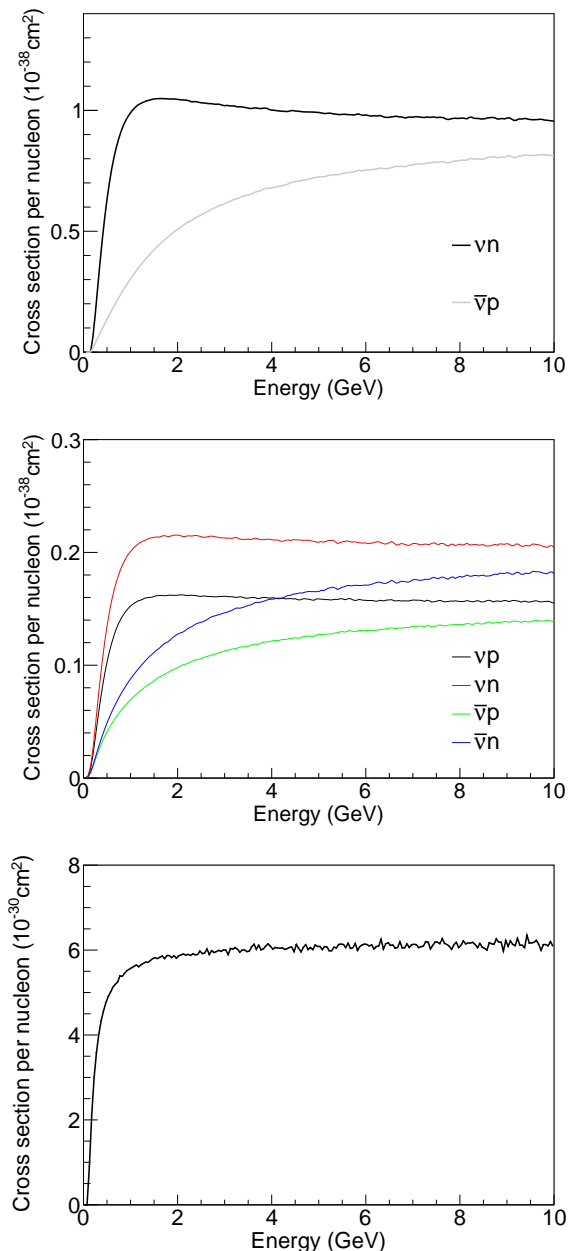


FIG. 2. Quasielastic cross section per nucleon as a function of incoming lepton energy of CC (top), NC (middle), and EM (bottom) interactions. The target nucleus is ^{16}O for CC and NC interactions and ^{12}C for EM interactions. Fermi momentum of $p_F = 209$ MeV is employed in calculations. The EM cross section is calculated with a cut of $Q^2 > 0.01$ GeV 2 .

default. The other is a dedicated nuclear deexcitation event generator NucDeEx [44, 45]. Radiative corrections are not implemented for electron scattering, while it is approximately implemented for CCQE interaction following Refs. [46, 47]. In the future, radiative correction could be incorporated, for example, through the universal implementation of radiative correction introduced in Ref. [48].

B. Single pion production based on the DCC model

The DCC model is employed to describe single pion production (1π) in electron scattering. The formalism is summarized in Refs. [14, 20]. In electron scattering, only 1π is implemented in NEUT, while the DCC model can describe double pion production. For both neutrino and electron interactions, NEUT assumes that the target nucleon moves with momentum below the Fermi surface with on-shell mass. The nucleon momentum is assumed to be uniformly distributed in the momentum phase space. Interactions are described in the nucleon rest frame, and the particle kinematics are then boosted to the laboratory frame. Pauli blocking can be optionally considered using a step-function, similar to that used in QE. In this study, the invariant mass is restricted to $W < 2.1$ GeV. Figure. 3 shows the 1π cross section for electrons according to the DCC model.

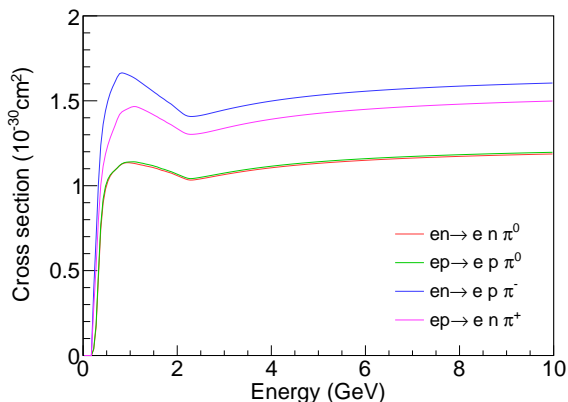


FIG. 3. Single pion production cross section for electrons based on the DCC model as a function of electron energy [14, 20]. The cross section is calculated with $W < 2.1$ GeV.

III. COMPARISON WITH INCLUSIVE ELECTRON SCATTERING DATA

This section discusses comparisons between NEUT predictions and inclusive electron scattering data on carbon and oxygen, $^{12}\text{C}(e, e')$ and $^{16}\text{O}(e, e')$. The NEUT implementation of the QE model was first validated by comparing it with numerical calculations by Ankowski *et al.* [13]. The NEUT simulations were found to be consistent with their numerical calculations, confirming the validity of the implementation. The impact of Coulomb potential and Pauli blocking on NEUT simulations was also investigated. Both effects were found to be small and negligible for the subsequent discussions. Details of these foundational studies are provided in Appendix B.

The NEUT simulations are compared with various experimental data at different electron energies and scat-

tering angles [49–56]. The results of $^{12}\text{C}(e, e')$ are shown in Figs. 4-8, and those of $^{16}\text{O}(e, e')$ are shown in Fig. 9. Two peaks corresponding to QE and 1π interactions are observed. Furthermore, it is observed that the NEUT simulation does not fully reproduce the QE peak in the datasets of low momentum transfer. This discrepancy is attributed to an effect beyond the PWIA, namely the distortion of the outgoing nucleon wave function by the nuclear potential [12, 13]. More details are discussed in Sec. III A.

In the region between QE and 1π , known as the “dip” region, the excess of data is visible. The excess is generally explained by multi-nucleon interaction, which is not yet implemented in the NEUT electron scattering. The solid (dashed) red line in Figs. 4-9 shows the 1π contribution without (with) Pauli blocking. This impact is small and negligible in the high-momentum transfer datasets where the 1π contribution is large. Although NEUT assumes that the target nucleon has on-shell mass, i.e., neglecting binding energy, there is overall good agreement with experimental data in the peak positions of 1π . Considering binding energy in 1π interactions is one of the important tasks for the future. Once this is achieved, the NEUT model can be evaluated further using the 1π region of electron scattering.

A. Extracting momentum-dependent binding energy correction

The QE peak shifts observed in Figs. 4-9 show the limitation of the simple PWIA prescription, which neglects the distortion of the struck nucleon wave function by the nuclear potential. These discrepancies can be addressed by applying a momentum-dependent binding energy correction extracted similarly to Ref. [12, 16]. The QE peaks in Figs. 4-9 are fitted with a Gaussian function for both NEUT simulations and experimental data. The peak shift $\Delta\omega$ is defined as

$$\Delta\omega = \omega_{data} - \omega_{neut}, \quad (17)$$

where ω_{data} (ω_{neut}) denotes the mean value of the Gaussian fitting of data (NEUT). The three-momentum transfer q_3 can be calculated with

$$\begin{aligned} Q^2 &= 2E(E - \omega_{data})(1 - \cos\theta), \\ q_3 &= \sqrt{Q^2 + \omega_{data}^2}, \end{aligned} \quad (18)$$

where E and θ denote the initial electron energy and scattering angle, respectively. The following four datasets are excluded from this analysis due to the absence of clear peaks: (200 MeV, 36°), (200 MeV, 60°), (240 MeV, 36°), and (320 MeV, 36°) on carbon.

Figure 10 shows an obtained relation between the peak shift $\Delta\omega$ and the three-momentum transfer q_3 . A clear positive correlation is observed between these two parameters. The peak shift deviates from zero and has

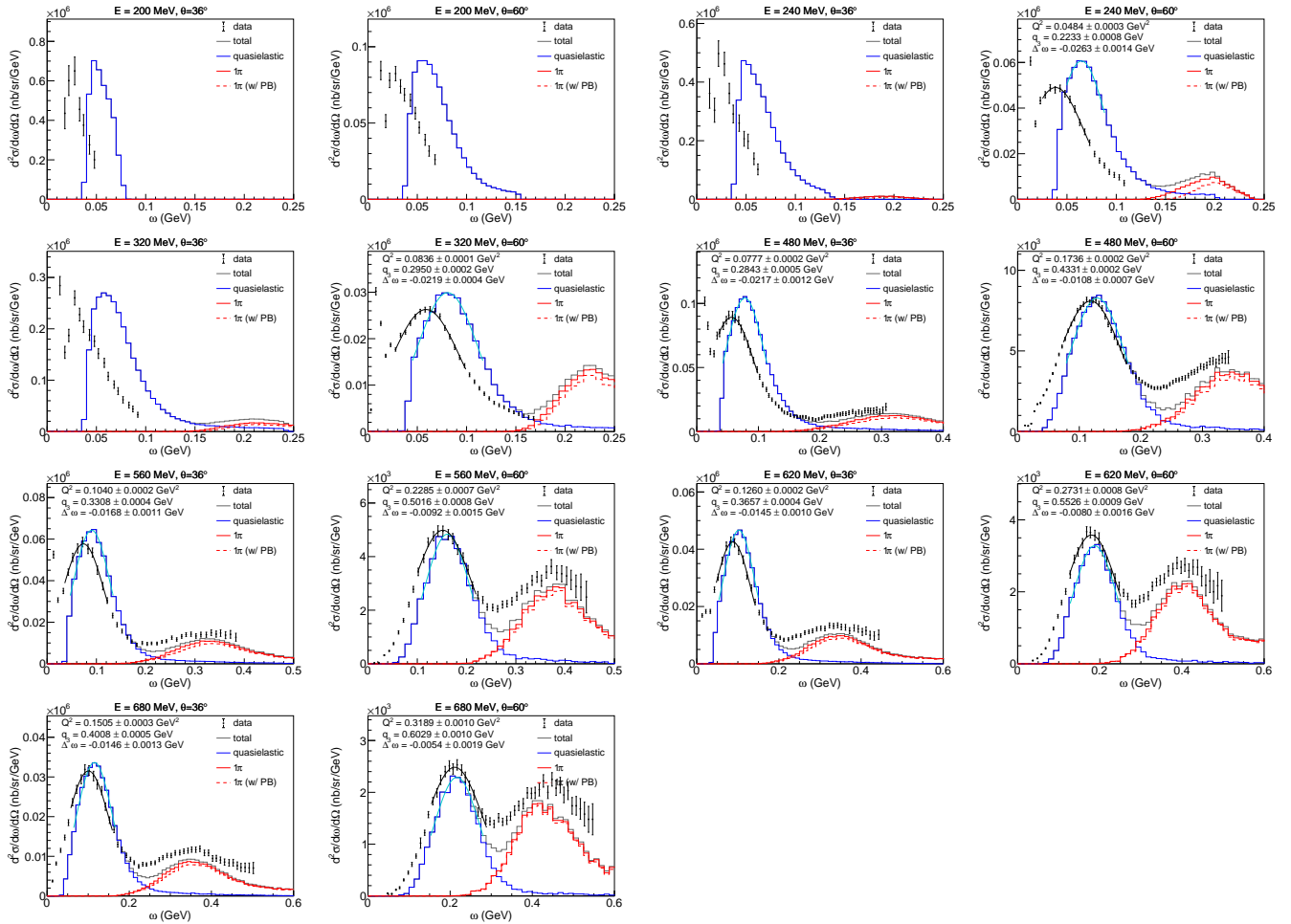


FIG. 4. Comparisons of inclusive electron scattering $^{12}\text{C}(e, e')$ cross section between NEUT and experimental data [50]. The figures are labeled by electron energy and scattering angle. The blue line shows the contribution of quasielastic and the red solid (dashed) line shows the contribution of single pion production without (with) Pauli blocking effect. The gray line shows the total cross section, summing QE and single pion production without Pauli blocking effect. The black (cyan) curved line on the QE peak shows the result of the Gaussian fitting discussed in Sec. III A. Parameters of Q^2 , q_3 , and $\Delta\omega$ written in the figures are defined as Eq. (17) and (18).

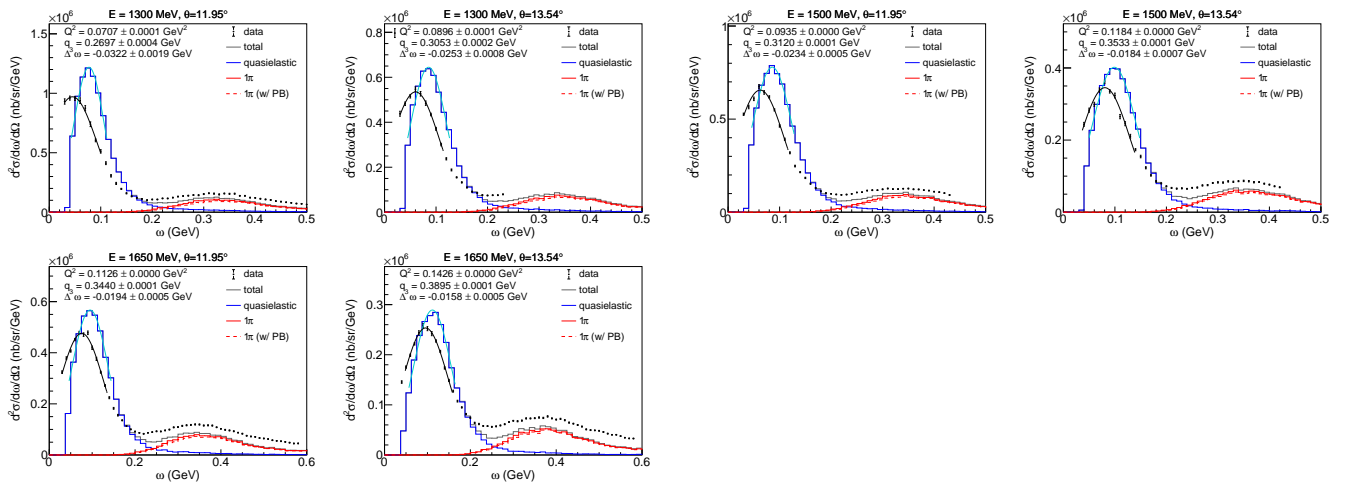


FIG. 5. The same as Fig. 4 but comparisons with different experimental data [51].

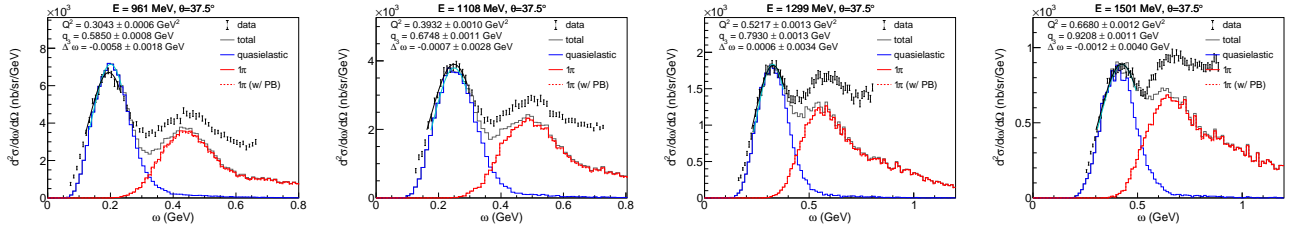


FIG. 6. The same as Fig. 4 but comparisons with different experimental data [52].

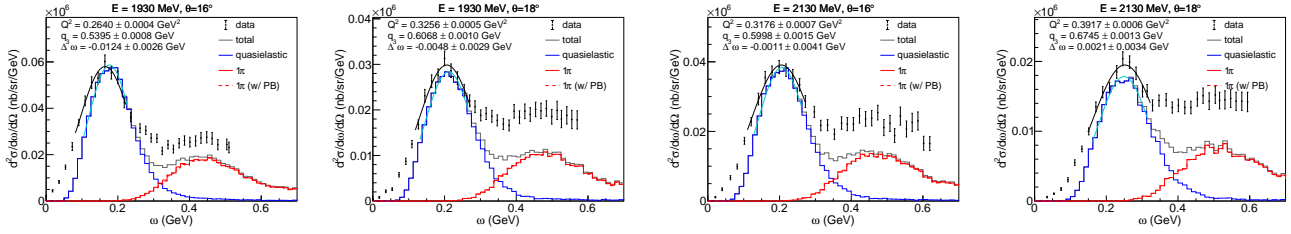


FIG. 7. The same as Fig. 4 but comparisons with different experimental data [53].

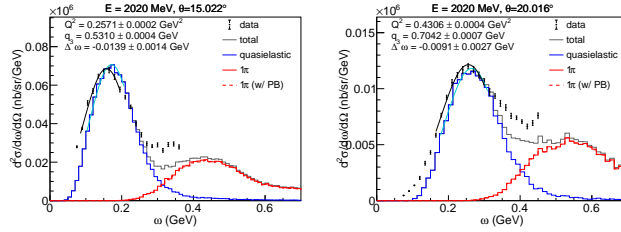


FIG. 8. The same as Fig. 4 but comparisons with different experimental data [54].

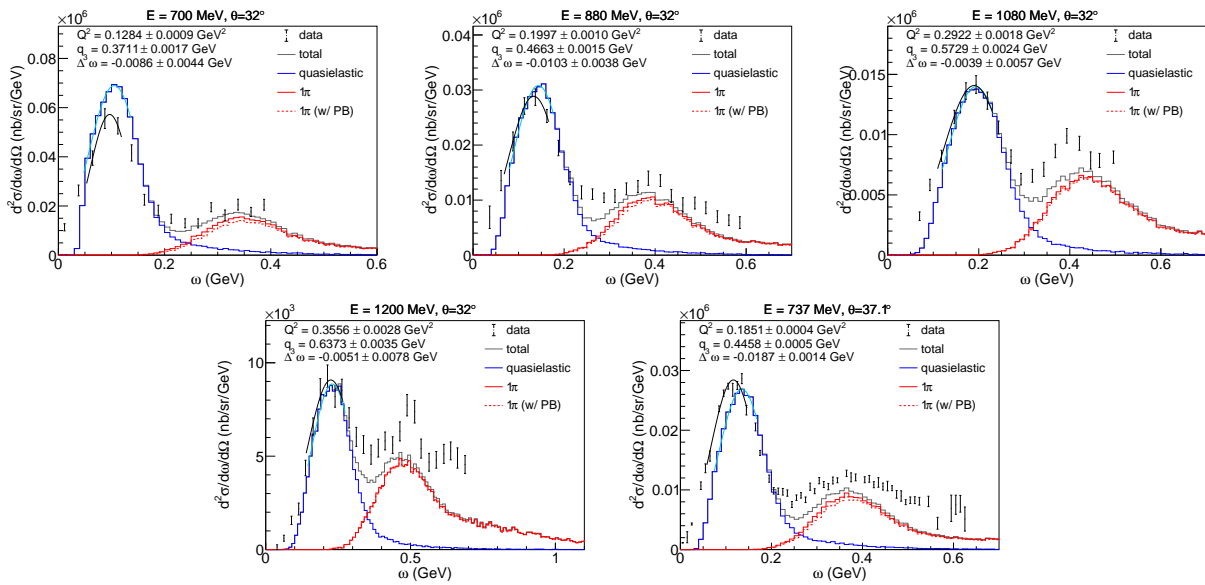


FIG. 9. The same as Fig. 4 but comparisons of inclusive electron scattering $^{16}\text{O}(e, e')$ cross section between NEUT and experimental data [55, 56].

a negative value in low momentum transfer, while it is saturated to zero in high momentum transfer. A similar trend is observed in numerical calculations based on the relativistic Fermi gas model [12]. This correlation is parameterized by fitting with a simple linear function $f(q_3) = aq_3 + b$. The following result is obtained when only the data on carbon is used.

$$\begin{aligned} a &= 0.0556 \pm 0.0021, \\ b &= -0.0386 \pm 0.0008 \text{ GeV}, \end{aligned} \quad (19)$$

which is the black solid line in Fig. 10. The errors denote the fitting uncertainties, including statistical uncertainty in NEUT and experimental uncertainty. The data for oxygen have relatively large uncertainties, with no clear differences from carbon. Significant differences appear in the correlation of these parameters for heavier nuclei such as ^{40}Ca , ^{56}Fe , and ^{208}Pb , but no significant differences are seen for carbon and oxygen [12]. When all data on carbon and oxygen are used, no significant change appears in the best-fit parameters as shown in Tab. I.

The derived function represents a correction to the binding energy, accounting for effects beyond the PWIA. It reduces the effective binding energy at lower momentum transfer. We can empirically introduce effects beyond the PWIA by correcting the binding energy using this function. More details are discussed in Sec. IV.

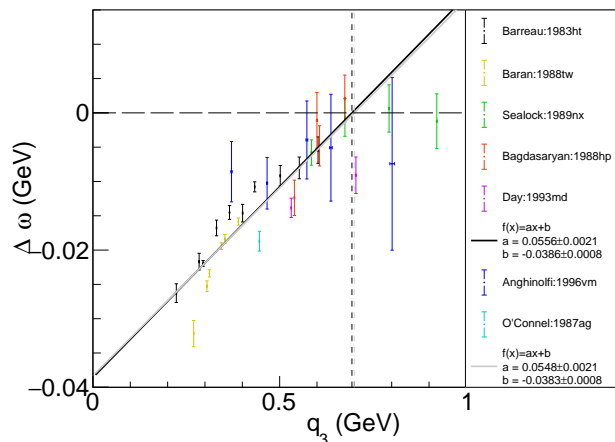


FIG. 10. Relation between the peak shift $\Delta\omega$ and three-momentum transfer q_3 . The dots represent the results of 31 datasets in total: The blue and cyan dots represent data on oxygen while others represent data on carbon. The solid black line represents the best fit by a linear function $f(q_3)$ with carbon data only, while the solid gray line represents that using all data of carbon and oxygen. The error bars represent the fitting uncertainty of Gaussian, mainly from the uncertainty of the experimental data.

1. Systematic uncertainties

The correction function derived above requires clarification: It assumes a Fermi momentum of 209 MeV, and neglects multi-nucleon interaction and deep inelastic scattering (DIS). The effects of the Coulomb potential and Pauli blocking on the determination of the correction function are negligibly small as discussed in Appendices B 2 and B 3. Varying the Fermi surface to $p_F = 221$ MeV, which is derived from electron scattering data based on Fermi gas model [57], results in a minor change comparable to the uncertainty, as shown in Tab. I. The DIS contribution to the QE peak is also negligible, as inferred from Ref. [6]. However, multi-nucleon interaction contributes significantly to the determination of the QE peak position as shown in Refs. [6, 14], Therefore, the result above, which neglects multi-nucleon interactions, may have some bias. An accurate assessment of this contribution requires the implementation of multi-nucleon interaction into NEUT, which is one of the significant future challenges. Instead of implementation, the impact of multi-nucleon interactions is investigated by using numerical calculations on carbon by Rocco *et al.* [14], which considers meson-exchange current (MEC).

Fig. 11 shows comparisons between NEUT simulations and experimental data, this time including the MEC contribution [14]. Including the MEC contribution improves the agreement between NEUT and the experimental data, particularly in the dip region. Also, by comparing the QE peak positions of Fig. 11 and Figs. 4-6, we can see the impact of MEC on the QE peak position of NEUT. By adding MEC contribution, the peak positions of NEUT shift toward higher energy transfer by several MeV. This shift is larger than that caused by other systematic factors, such as Pauli blocking. Consequently, the absence of MEC likely contributes as a primary systematic uncertainty in the analysis above. As inferred from the figures, the magnitude of moving depends on the datasets, i.e., momentum transfer.

The correlation between the peak shift and three-momentum transfer is re-evaluated, including the MEC contribution calculated by Rocco *et al.* Figure 12 shows the results, noting that the MEC calculations are limited to certain datasets. By fitting the correlation with a linear function, the following results are obtained (see also Tab. I):

$$\begin{aligned} a &= 0.0436 \pm 0.0035, \\ b &= -0.0365 \pm 0.0013 \text{ GeV}, \end{aligned} \quad (20)$$

with larger uncertainties due to the limited datasets. It is observed that the impact of MEC makes a major difference in determining correction function compared to Pauli blocking and Coulomb potential. This result is used to assess the systematic uncertainty of the MEC contribution in the following discussion.

TABLE I. The best-fit parameters of momentum-dependent binding energy correction $f(q_3) = aq_3 + b$ with four analysis conditions. The results are written with different treatment of Fermi momentum p_F , meson-exchange current (MEC) contribution, and ^{16}O data.

Fermi momentum	MEC	^{16}O data	a	b (GeV)
$p_F = 209 \text{ MeV}$	None	None	0.0556 ± 0.0021	-0.0386 ± 0.0008
	None	Yes	0.0548 ± 0.0021	-0.0383 ± 0.0008
	Yes	None	0.0436 ± 0.0035	-0.0365 ± 0.0013
$p_F = 221 \text{ MeV}$	None	None	0.0576 ± 0.0021	-0.0395 ± 0.0008

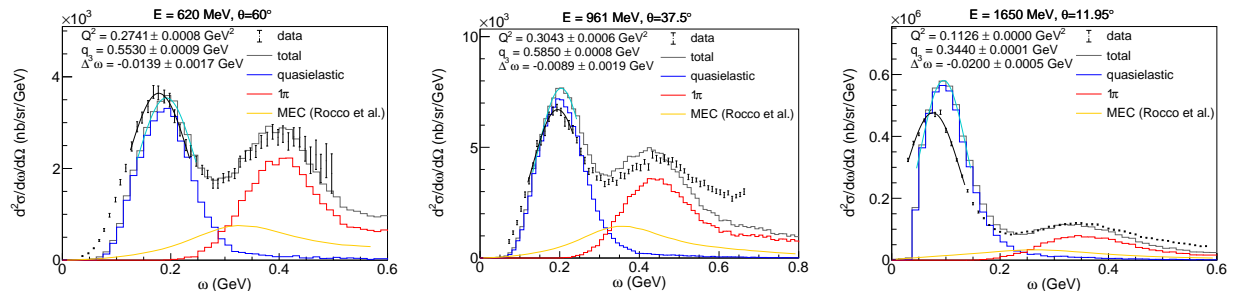


FIG. 11. Comparisons of inclusive electron scattering $^{12}\text{C}(e, e')$ cross section between NEUT and experimental data [50–52]. The orange lines represent the numerical calculation of meson-exchange current by Rocco *et al.* [14]. The gray line shows the total cross section including the meson-exchange current.

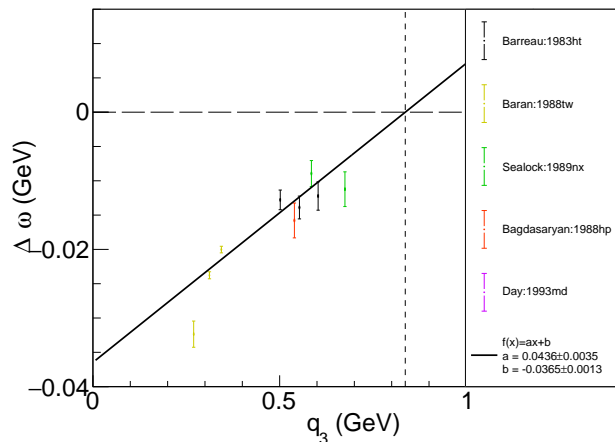


FIG. 12. The same as Fig. 10, but meson-exchange current contribution calculated by Rocco *et al.* is added.

IV. APPLYING MOMENTUM-DEPENDENT BINDING ENERGY CORRECTION

The momentum-dependent binding energy correction, derived in Sec. III A, is applied to account for effects beyond PWIA empirically. The correction $\Delta\tilde{E}$, as a function of three-momentum transfer q_3 , is defined as follows:

$$\Delta\tilde{E} = \begin{cases} f(q_3) & (f(q_3) \leq 0), \\ 0 & (f(q_3) > 0), \end{cases} \quad (21)$$

where $f(q_3)$ is the best-fit function shown in Eq. (19), which is extracted from carbon data only. Since no clear

differences are observed between carbon and oxygen, this best-fit function is applied to both carbon and oxygen. Above a certain three-momentum transfer q_3 , the function $f(q_3)$ becomes positive, and $\Delta\tilde{E}$ is truncated to zero. That is, no correction is applied at high-momentum transfers. This truncation reflects the fact that the peak shift is not observed in high-momentum transfer datasets, i.e., the PWIA is sufficiently accurate in this region. The differential cross section is then calculated by redefining the binding energy, shown in Eq. 4, as

$$\tilde{E} \rightarrow \tilde{E} + \Delta\tilde{E}. \quad (22)$$

This correction reduces the binding energy since $\Delta\tilde{E}$ has a negative value, which could potentially lead to an unphysical negative binding energy. A truncation is introduced to maintain physical consistency:

$$\tilde{E} = \begin{cases} 0 & (\tilde{E} < 0), \\ \tilde{E} & (\tilde{E} \geq 0), \end{cases} \quad (23)$$

where the negative binding energy is not allowed.

A. Electron scattering

The correction is first applied to electron scattering in order to investigate its effectiveness. Figure 13 shows the results after applying the correction. Compared to the results before applying the correction (Fig. 4), the QE peak positions shift, and the peak shift relative to the experimental data disappears within the uncertainty, as expected.

However, NEUT still disagrees with the experimental data in terms of the QE peak height. NEUT tends to over-predict the peak height in datasets with low momentum transfer, which is also observable before applying the correction, as shown in Fig. 4. Since this correction reduces the effective binding energy, it does not lead to a reduction in the cross section. To improve agreement, factors that reduce the cross-section at low momentum transfer are needed, beyond merely shifting the energy transfer distribution. A theory-driven correction discussed in Ref. [13] shows better agreement with the experimental data in both peak position and height, compared to the results presented in this paper. This is because they account for the shift of the QE peak position using the real part of the optical potential, and a broadening of the cross section induced by FSI. The correction discussed here is empirical and has limitations in its ability to accurately reproduce the experimental data. The inclusion of such a theory-driven correction is one of the essential challenges for future work.

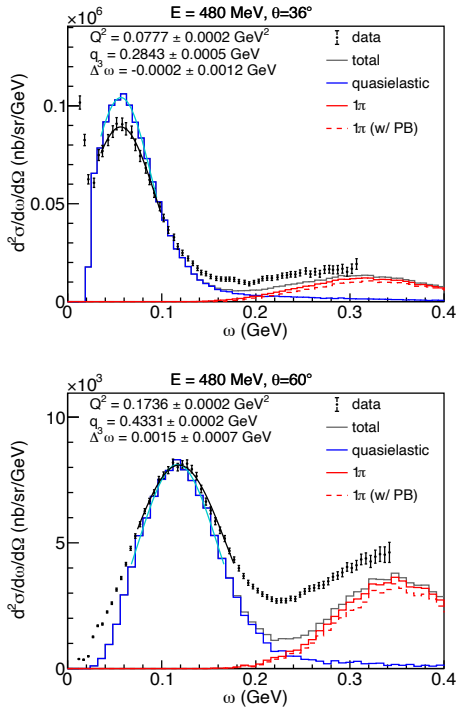


FIG. 13. The same as Fig. 4 but after applying the momentum-dependent binding energy correction using Eq. 19.

B. Neutrino interactions

The correction is applied to neutrino scattering in order to evaluate its impact on neutrino oscillation experiments. The neutrino energy can be reconstructed from the measured charged lepton kinematics by assuming charged-current quasielastic (CCQE) interactions, as

described in the Super-Kamiokande analysis of the T2K experiment [3]. The neutrino energy in CCQE interactions can be reconstructed using energy and momentum conservation:

$$E_\nu^{rec} = \frac{2E_l \tilde{M} - (m_l^2 + \tilde{M}^2 - M_f^2)}{2(\tilde{M} - E_l + p_l \cos \theta_l)}, \quad (24)$$

$$\tilde{M} = M_i - E_b,$$

where E_l , p_l , m_l , and $\cos \theta_l$ denote outgoing charged lepton energy, momentum, mass, and scattering angle, respectively. M_i and M_f are the initial and final nucleon masses, and E_b is binding energy. For the following discussion, the same binding energy of $E_b = 27$ MeV for ^{16}O , as assumed in T2K [3], is used.

Figure 14 shows the reconstructed neutrino energy of ν_μ and $\bar{\nu}_\mu$ CCQE interactions on oxygen for a true neutrino energy of 600 MeV. The correction derived from electron scattering results in a significantly different distribution. A sizable change in peak positions is observed, approximately 20 MeV. The peak positions of the distribution for different true neutrino energies and neutrino flavors are summarized in Tab. II. The peak position shift does not show a clear dependence on the true neutrino energy and neutrino flavors.

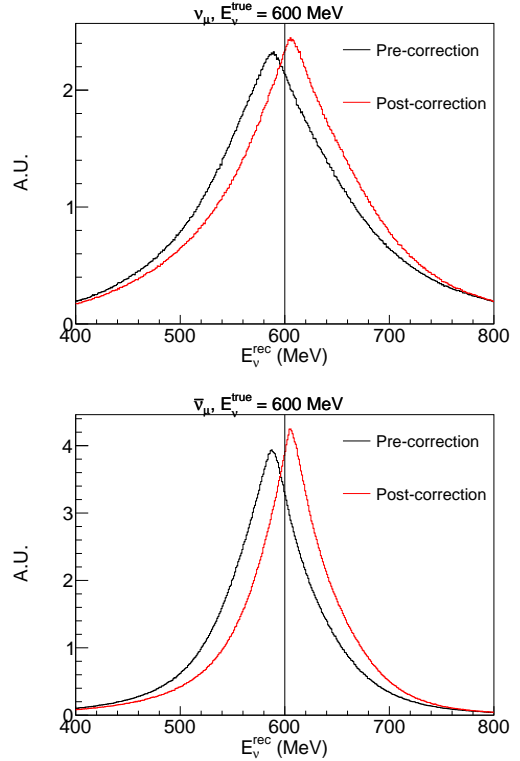


FIG. 14. Reconstructed neutrino energy distribution in ν_μ (top) and $\bar{\nu}_\mu$ (bottom) CCQE interactions on oxygen at true neutrino energy of 600 MeV. The black and red lines show the calculations before and after applying the momentum-dependent binding energy correction, respectively.

TABLE II. Peak positions of reconstructed neutrino energy distribution before and after applying the binding energy correction for different true neutrino energies and neutrino flavors. All values are written in units of MeV.

flavor	correction	True neutrino energy				
		200	400	600	800	1000
ν_μ	before	191	389	588	788	988
ν_μ	after	209	407	607	806	1006
ν_e	before	189	388	588	788	988
ν_e	after	207	407	606	806	1006
$\bar{\nu}_\mu$	before	189	388	588	788	988
$\bar{\nu}_\mu$	after	207	406	606	806	1006
$\bar{\nu}_e$	before	187	387	587	787	987
$\bar{\nu}_e$	after	205	405	606	806	1006

The impact of the major systematic uncertainty, namely the MEC contribution, is further investigated using the best-fit function in Eq. 20, which accounts for the MEC contribution. While including MEC leads to a noticeable difference in the correction function, it results in only minor shifts, approximately ± 1 MeV in the peak positions of the reconstructed neutrino energy.

The observed 20 MeV shift in the E_ν^{rec} distribution is consistent with Ref. [12], which introduced a similar correction to that in this paper. However, a theory-based correction for the distortion effect discussed in Ref. [13] shows larger shifts of about 30 MeV. This indicates that the empirical correction used in this analysis cannot describe the behavior of the approach of Ref. [13], calling for its improved implementation in the future.

V. CONCLUSION AND PROSPECTS

This paper presents the successful implementation of electron scattering in the neutrino event generator NEUT for two interaction modes: QE and 1π . A framework is established to extend NEUT for simulating electron scattering, ensuring compatibility with the existing framework. It enables direct evaluations of NEUT models by using abundant high-precision electron scattering data. An SF-based model is implemented for QE interaction. This model can describe both neutrino and electron scatterings by changing only the coupling constant and form factors. For 1π interactions, the DCC model is employed, with code provided by the authors that describes both neutrino and electron scatterings.

The NEUT QE implementation is validated through comparisons with numerical calculations by Ankowski *et al.* The NEUT predictions are compared with inclusive electron scattering data of $^{12}\text{C}(e, e')$ and $^{16}\text{O}(e, e')$. A shift in the QE peak positions is observed, which strongly depends on momentum transfer, yielding significant shifts for low momentum transfers of $q_3 \lesssim 0.6$ GeV, while it is negligible for high momentum transfer. The

correlation of the peak shift and the momentum transfer is parameterized by a linear function.

The result can be used as a correction term to the binding energy, empirically introducing effects beyond the PWIA. To evaluate its impact on neutrino oscillation experiments, the correction is applied to neutrino CCQE interactions. We observed sizable shifts in reconstructed neutrino energy distribution of approximately 20 MeV between 200 and 1000 MeV for true neutrino energies. Although this paper introduces an empirical correction to the binding energy, a theory-driven correction, as discussed in Ref. [13], would be preferable. This is one possible future development of NEUT.

This paper primarily focuses on the implementation details and discussions of QE in inclusive scattering (e, e'). There are plenty of exciting topics to be studied in the future. Comparisons with semi-inclusive measurements, such as $(e, e'p)$ and $(e, e'\pi)$, provide abundant information for validating FSI cascade models, as discussed in Ref. [7]. Investigating models of 1π is also an interesting topic. Currently, NEUT assumes that the target nucleon has on-shell mass. We plan to revisit this assumption using electron scattering data. Also, implementing other interaction channels such as multi-nucleon interactions and DIS will be a significant future challenge. Completing the implementation of electron scattering will provide deeper insights into nuclear models and their connection to neutrino interactions.

The code developed in this study will be included in the upcoming NEUT release. Thus, further discussions on electron scattering using NEUT are expected to proceed smoothly. Such discussions can be extended straightforwardly to neutrino interactions and to neutrino physics analyses using NEUT, e.g., analyses at Super-Kamiokande [58], T2K [3], and Hyper-Kamiokande [59] experiments. The study presented here is expected to serve as a foundational step for enhancing future neutrino oscillation analyses in these experiments using electron scattering.

ACKNOWLEDGMENTS

This work was supported by JSPS KAKENHI Grant No. 23KJ0319. The author expresses deep gratitude to the host researcher of this JSPS fellowship, Prof. Yoshinari Hayato, for his invaluable assistance in improving the manuscript. The author thanks Dr. Artur M. Ankowski for his insightful comments on the manuscript and for providing his numerical calculation results, which were essential for validating the implementation. The author also thanks Prof. Toru Sato and Dr. Noemi Rocco for sharing their numerical calculations on MEC. The author finally thanks T2K Neutrino Interaction Working Group for their valuable discussions.

Appendix A: Event generation process of quasielastic interactions in NEUT

In the event generation process of quasielastic interactions, the elementary cross section described in Eq. (7) is transformed into the center-of-mass variables. The velocity of the center-of-mass frame \mathbf{v} and the Lorentz factor γ are expressed as

$$\begin{aligned} \mathbf{v} &= \frac{\mathbf{p} + \mathbf{k}}{E_k + M - \tilde{E}} = \frac{\mathbf{p} + \mathbf{k}}{y}, \\ y &\equiv E_k + M - \tilde{E}, \\ \gamma &= \frac{1}{\sqrt{1 - \mathbf{v}^2}}, \end{aligned} \quad (\text{A1})$$

where y represents the total energy of the center-of-mass frame. The Mandelstam variable s of the center-of-mass

frame is defined by

$$s = y^2 - (\mathbf{p} + \mathbf{k})^2. \quad (\text{A2})$$

Since the Mandelstam variable s is Lorentz invariant, the momentum of outgoing lepton in the center-of-mass frame, \mathbf{k}'_{com} , is determined by momentum conservation as

$$|\mathbf{k}'_{\text{com}}| = \sqrt{\frac{(s + m^2 - M^2)^2}{4s} - m^2}, \quad (\text{A3})$$

where m is the outgoing lepton mass. Finally, the total cross section in terms of the center-of-mass variables is expressed as

$$\frac{d\sigma_{\text{tot}}}{dQ^2} = \frac{C}{E_k} \int d^3p d\tilde{E} P_{\text{hole}}(\mathbf{p}, \tilde{E}) \int \frac{L_{\mu\nu} H^{\mu\nu}}{E_p E_{p'} E_{k'}} \frac{\sqrt{1 + (\gamma^2 - 1)(\cos^2 \theta_{\text{com}} - 1)}}{|\mathbf{v}_{\mathbf{k}'} - \mathbf{v}_{\mathbf{p}'}|} |\mathbf{k}'_{\text{com}}|^2 d\phi_{\text{com}} d\cos \theta_{\text{com}}, \quad (\text{A4})$$

where $\mathbf{v}_{\mathbf{k}'}$ and $\mathbf{v}_{\mathbf{p}'}$ denote the velocities of outgoing lepton and nucleon in the laboratory frame, respectively, and θ_{com} and ϕ_{com} represent the zenith and azimuth angles, respectively, between outgoing lepton in the center-of-mass frame and velocity of the center-of-mass frame, i.e.,

$$\begin{aligned} \mathbf{v}_{\mathbf{k}'} &= \mathbf{k}'/E_{k'}, \\ \mathbf{v}_{\mathbf{p}'} &= \mathbf{p}'/E_{p'}, \\ \cos \theta_{\text{com}} &= \frac{\mathbf{v} \cdot \mathbf{k}'_{\text{com}}}{|\mathbf{v}| |\mathbf{k}'_{\text{com}}|}. \end{aligned} \quad (\text{A5})$$

The event generation proceeds through the following steps:

- The removal energy \tilde{E} and the momentum of the target nucleon \mathbf{p} are sampled according to the SF.
- The outgoing lepton energy in the center-of-mass frame, $|\mathbf{k}'_{\text{com}}|$, is computed using Eq. (A3).
- The angles θ_{com} and ϕ_{com} are sampled randomly.
- The total cross section is calculated from Eq. (A4).
- The weights are determined by comparing the pre-calculated maximum cross section with the cross section being currently generated. Events are either accepted or rejected based on their weights using a random sampling method.

Appendix B: Checks on the implementations and behaviours of quasielastic scattering

1. Validation using numerical calculation

The implementation of the QE model in NEUT is validated by comparing it with theoretical numerical calculations by Ankowski *et al.* [13]. The NEUT simulation gives good agreement with the numerical calculation, with a deviation of less than $\pm 5\%$ around peak region, as shown in Fig. 15. The target nucleus is carbon, and the same Coulomb potential of 3.1 MeV and a step-function Pauli blocking with $p_F = 209$ MeV are applied in these calculations. The deviation observed at the rising edge of the peak may result from slight differences in parameters such as nucleon and lepton masses. Other datasets also show good consistency. These results show the validity of NEUT implementation.

2. Impact of the Coulomb potential

The impact of Coulomb potential $|V_{\text{eff}}|$ to NEUT simulation is also investigated. Figure 16 shows the cross section predicted by NEUT with and without the Coulomb potential. Considering the Coulomb effect, the peak height decreases by a few percent, with a slight shift in the peak position of approximately +0.6 MeV. The impact of the Coulomb potential is negligible in the analysis in Sec. III A.

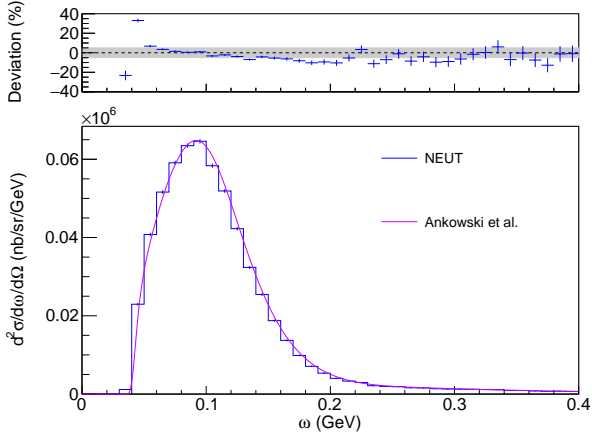


FIG. 15. Comparisons of quasielastic electron scattering $^{12}\text{C}(e, e')$ cross section between NEUT (blue) and numerical calculation by Ankowski *et al.* (violet) [13]. The electron energy is 560 MeV and the scattering angle is $\theta = 36^\circ$. The upper panel shows deviation from the numerical calculation, and the gray box represents $\pm 5\%$ region. The error bar denotes the statistical error of NEUT simulation.

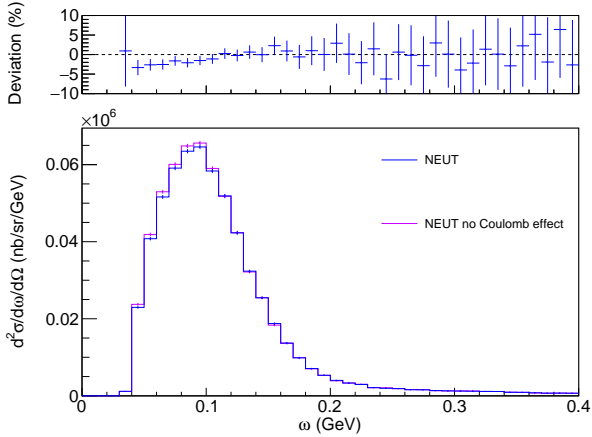


FIG. 16. The same dataset as Fig. 15, but a comparison between NEUT simulations with (blue) and without (violet) considering the Coulomb potential. The upper panel shows deviation from one without the Coulomb potential.

3. Impact of Pauli blocking

The impact of Pauli blocking is evaluated by varying the Fermi surface p_F as shown in Fig. 17. The Pauli blocking effect changes both the normalization and shape of the cross sections. It is clear that simply varying the Fermi surface does not adequately explain the discrepancies with the data. The impact is significant in the datasets of low momentum transfer while becoming negligible in high momentum transfer datasets of $Q^2 \gtrsim 0.1 \text{ GeV}^2$ and $q_3 \gtrsim 0.3 \text{ GeV}$. It is confirmed that varying the Fermi surface between $p_F = 209 \text{ MeV}$ and $p_F = 221 \text{ MeV}$ has only a minor impact on the correction function as shown in Tab. I.

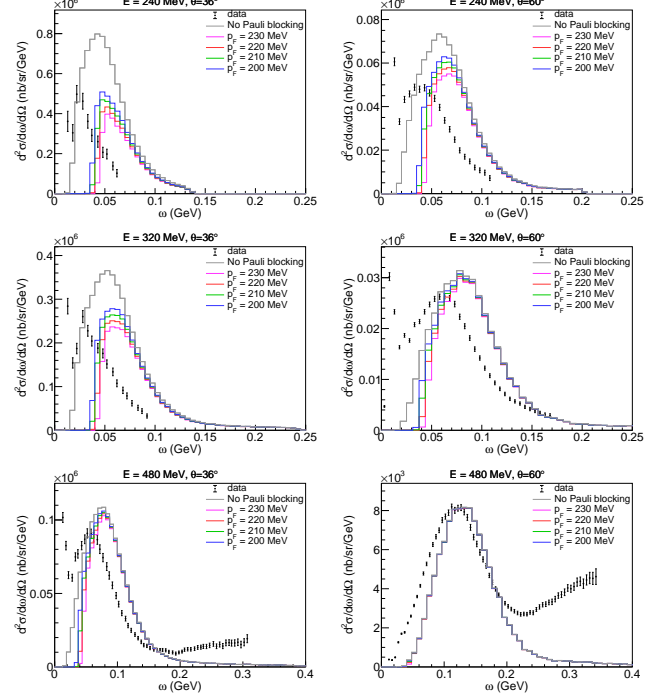


FIG. 17. Impact of Pauli blocking on $^{12}\text{C}(e, e')$ cross section predicted by NEUT. The NEUT simulations consider quasielastic scattering only. The data is from Ref. [50]. The gray lines show the results without applying Pauli blocking, and the other lines show the results of varying the Fermi surface $p_F = 200, 210, 220, 230 \text{ MeV}$.

[1] K. Abe *et al.*, The European Physical Journal C **83**, 782 (2023).
 [2] M. A. Acero *et al.* (The NOvA Collaboration), Phys. Rev. D **106**, 032004 (2022).
 [3] K. Abe *et al.* (The T2K Collaboration), Phys. Rev. D **96**, 092006 (2017).
 [4] A. A. Aguilar-Arevalo *et al.* (MiniBooNE Collaboration), Phys. Rev. Lett. **120**, 141802 (2018).

[5] E. Marzec *et al.*, (2024), arXiv:2409.01383 [hep-ex].
 [6] A. Papadopoulou *et al.* ($e4\nu$ Collaboration), Phys. Rev. D **103**, 113003 (2021).
 [7] M. Khachatryan *et al.* ($e4\nu$ Collaboration), Nature **599**, 565 (2021).
 [8] J. Żmuda, K. Graczyk, C. Juszczak, and J. Sobczyk, Acta Phys. Pol. B **46**, 2329 (2015).

- [9] R. D. Banerjee, A. M. Ankowski, K. M. Graczyk, B. E. Kowal, H. Prasad, and J. T. Sobczyk, *Phys. Rev. D* **109**, 073004 (2024).
- [10] J. Isaacson, W. I. Jay, A. Lovato, P. A. N. Machado, and N. Rocco, *Phys. Rev. D* **107**, 033007 (2023).
- [11] A. Bodek and M. E. Christy, *Phys. Rev. C* **106**, L061305 (2022).
- [12] A. Bodek and T. Cai, *The European Physical Journal C* **79**, 293 (2019).
- [13] A. M. Ankowski, O. Benhar, and M. Sakuda, *Phys. Rev. D* **91**, 033005 (2015).
- [14] N. Rocco, S. X. Nakamura, T.-S. H. Lee, and A. Lovato, *Phys. Rev. C* **100**, 045503 (2019).
- [15] Y. Hayato and L. Pickering, *Eur. Phys. J. Special Topics* **230**, 4469 (2021).
- [16] S. Dolan *et al.*, (2023), arXiv:2301.09195 [hep-ex].
- [17] J. McElwee, Ph.D. thesis, University of Sheffield (2022).
- [18] O. Benhar, A. Fabrocini, S. Fantoni, and I. Sick, *Nucl. Phys. A* **579**, 493 (1994).
- [19] O. Benhar, N. Farina, H. Nakamura, M. Sakuda, and R. Seki, *Phys. Rev. D* **72**, 053005 (2005).
- [20] S. X. Nakamura, H. Kamano, and T. Sato, *Phys. Rev. D* **92**, 074024 (2015).
- [21] <https://www.rcnp.osaka-u.ac.jp/~anl-osk/>.
- [22] C. Juszczak, J. A. Nowak, and J. T. Sobczyk, *Nucl. Phys. B Proc. Suppl.* **159**, 211 (2006).
- [23] A. P. Furmanski, Ph.D. thesis, University of Warwick (2015).
- [24] A. M. Ankowski, *Phys. Rev. C* **86**, 024616 (2012).
- [25] W. Alberico, S. Bilenky, and C. Maieron, *Phys. Rep.* **358**, 227 (2002).
- [26] S. F. Pate, D. W. McKee, and V. Papavassiliou, *Phys. Rev. C* **78**, 015207 (2008).
- [27] E. Leader, A. V. Sidorov, and D. B. Stamenov, *Phys. Rev. D* **84**, 014002 (2011).
- [28] A. M. Ankowski and O. Benhar, *Phys. Rev. D* **88**, 093004 (2013).
- [29] S. Abe *et al.* (KamLAND Collaboration), *Phys. Rev. D* **107**, 072006 (2023).
- [30] R. Bradford, A. Bodek, H. Budd, and J. Arrington, *Nucl. Phys. B Proc. Suppl.* **159**, 127 (2006).
- [31] P. Guèye *et al.*, *Phys. Rev. C* **60**, 044308 (1999).
- [32] L. Wan *et al.* (Super-Kamiokande Collaboration), *Phys. Rev. D* **99**, 032005 (2019).
- [33] S. Sakai *et al.* (Super-Kamiokande Collaboration), *Phys. Rev. D* **109**, L011101 (2024).
- [34] M. Harada *et al.*, *The Astrophysical Journal Letters* **951**, L27 (2023).
- [35] V. Alexakhin *et al.*, *Phys. Lett. B* **647**, 8 (2007).
- [36] K. Ueno, Ph.D. thesis, Tokyo U. (2012).
- [37] A. M. Ankowski, O. Benhar, T. Mori, R. Yamaguchi, and M. Sakuda, *Phys. Rev. Lett.* **108**, 052505 (2012).
- [38] T. De Forest, *Nucl. Phys. A* **392**, 232 (1983).
- [39] C. Llewellyn Smith, *Phys. Rep.* **3**, 261 (1972).
- [40] A. M. Ankowski, O. Benhar, and M. Sakuda, *Phys. Rev. C* **110**, 054612 (2024).
- [41] R. Subedi *et al.*, *Science* **320**, 1476 (2008).
- [42] E. Piassetzky, M. Sargsian, L. Frankfurt, M. Strikman, and J. W. Watson, *Phys. Rev. Lett.* **97**, 162504 (2006).
- [43] K. Kobayashi *et al.*, (2006), arXiv:nucl-ex/0604006 [nucl-ex].
- [44] S. Abe, *Phys. Rev. D* **109**, 036009 (2024).
- [45] <https://github.com/SeishoAbe/NucDeEx>.
- [46] O. Tomalak, Q. Chen, R. J. Hill, and K. S. McFarland, *Nature Communications* **13**, 5286 (2022).
- [47] O. Tomalak, Q. Chen, R. J. Hill, K. S. McFarland, and C. Wret, *Phys. Rev. D* **106**, 093006 (2022).
- [48] J. T. Vidal, A. Ashkenazi, L. B. Weinstein, P. Blunden, S. Dytman, and N. Steinberg, (2024), arXiv:2409.05736 [hep-ex].
- [49] O. Benhar, D. Day, and I. Sick, (2006), arXiv:nucl-ex/0603032 [nucl-ex].
- [50] P. Barreau *et al.*, *Nucl. Phys.* **A402**, 515 (1983).
- [51] D. T. Baran *et al.*, *Phys. Rev. Lett.* **61**, 400 (1988).
- [52] R. M. Sealock *et al.*, *Phys. Rev. Lett.* **62**, 1350 (1989).
- [53] D. S. Bagdasaryan *et al.*, YERPHI-1077-40-88.
- [54] D. B. Day *et al.*, *Phys. Rev.* **C48**, 1849 (1993).
- [55] M. Anghinolfi *et al.*, *Nucl. Phys.* **A602**, 405 (1996), nucl-th/9603001.
- [56] J. S. O'Connell *et al.*, *Phys. Rev.* **C35**, 1063 (1987).
- [57] E. J. Moniz, I. Sick, R. R. Whitney, J. R. Ficenece, R. D. Kephart, and W. P. Trower, *Phys. Rev. Lett.* **26**, 445 (1971).
- [58] T. Wester *et al.* (The Super-Kamiokande Collaboration), *Phys. Rev. D* **109**, 072014 (2024).
- [59] K. Abe *et al.* (Hyper-Kamiokande proto-collaboration), (2018), arXiv:1805.04163 [physics.ins-det].